A 2.5D peridynamic model for turnout rail crack propagation under wheel rolling contact action

Xiaochuan Ma✉, Xianghe Wang, Linya Liu, Weibin Yin, Yajie Wang, Qi Zeng

Cite this article: Ma XC, Wang XH, Liu LY, et al. *Friction* 2025, **13**(12): 9441072. https://doi.org/10.26599/FRICT.2025.9441072

ABSTRACT: Based on the ordinary state-based peridynamics (OSB PD) theory, a 2.5-dimensional (2.5D) PD model for rail crack propagation in railway turnouts was proposed. First, a two-dimensional (2D) model for rail crack propagation in railway turnouts was constructed, with two types of 2.5D additional constraints for crack opening and cross section proposed on the basis of the 2D model. The 2.5D PD model for rail crack propagation in railway turnouts could thus be established. A fatigue crack propagation experiment was subsequently carried out on the U71Mn turnout rail material. The bond fatigue failure condition of the turnout rail material was established on the basis of the experimental results. Finally, the accuracy of the structural deformation and bond fatigue failure conditions was verified. The simulation results for rail crack propagation were compared with field observations and then analyzed in detail. These results show that the proposed 2.5D PD model can be used to accurately simulate the characteristics and rules for rail crack propagation in railway turnouts.

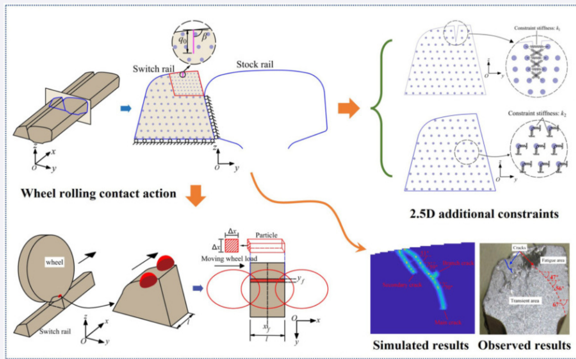

KEYWORDS: wheel–rail rolling contact; crack propagation; turnout rail; peridynamic model; fatigue fracture

1 Introduction

Railway turnout is a key part of railway infrastructure, enabling trains to carry out track switching and cross-track running. Under the action of a cyclic train load, cracks gradually appear in turnout rails after prolonged use. With increasing service time, these cracks expand further, resulting in stripping and chipping of the turnout rail. In extreme cases, this can even lead to rail fracture, seriously threatening the safety of the train. Therefore, it is highly important to study the fatigue crack propagation behavior of turnout rails, as this can reduce the railway maintenance costs, prolong rail service life, and ensure the safety of train operation.

In terms of fatigue failure in turnout rails, some researchers have used experimental methods to study this phenomenon. For example, Zuo et al. [1, 2] designed a testbed that included a full-scale turnout and a bogie wagon, and proposed a method for processing vibration data. This testbed can be used to monitor collapse damage on the rail surface of a turnout. Cornish et al. [3] conducted real-time monitoring of 4 turnouts on a British railway system and analyzed the effects of rail vibration acceleration and strain accumulation on rail failure. Wang et al. [4] studied different types of defects, microstructures of spalling materials, and wear conditions of a Chinese turnout switch rail. Looking primarily at Hadfield austenitic steel turnout rails, Luo et al. [5] used optical microscopy (OM) and scanning electron microscopy (SEM) techniques to analyze the causes of stripping and chipping damage to turnout rails. A ball-on-disc sliding wear test was conducted to evaluate the influence of hardening on rail fatigue wear performance. Zhang et al. [6] also used OM and SEM techniques to analyze the microstructure of the rail surface on a failed bainitic steel turnout. Eck et al. [7] tested the impact resistance, tensile strength, and fatigue resistance of five different rail turnout materials under the same conditions.

Experimental methods are often too time-consuming. Furthermore, owing to the complex structural characteristics of railway turnouts, the experimental conditions required are relatively strict. As a result, several researchers have used numerical simulations to study rail fatigue failure in railway turnouts. For example, Guo et al. [8] established a 3D elastic–plastic finite element model for the study of the nonlinear properties of materials and their dynamic impact on wheels and analyzed the deformation and damage caused by turnout rails. Zhu et al. [9] established a coupled dynamic vehicle–turnout rigid-flexible model and systematically analyzed the fatigue failure of a straight switch during turnout under complex random loads. Ma et al. [10] conducted numerical simulations and predictions of rolling contact fatigue failure in a turnout rail on the basis of coupled vehicle–turnout system dynamics and wheel–rail rolling

State Key Laboratory of Performance Monitoring and Protecting of Rail Transit Infrastructure, East China Jiaotong University, Nanchang 330013, China.

✉ Corresponding author. E-mail: rw.ma@ecjtu.edu.cn

Received: June 17, 2024; Revised: September 7, 2024; Accepted: January 22, 2025

contact theory. Six et al. [11] predicted the cumulative damage caused to a rail in a turnout. Qian et al. [12] analyzed the rail wear and damage when a CRH2 train passed through a turnout. Nielsen et al. [13] proposed a numerical method for calculating the cumulative wear and fatigue on turnout rails; this method can then be used to predict the fatigue failure of the rail. Xin et al. [14] proposed a numerical method for fatigue crack initiation analysis and service lifetime prediction of a railway turnout.

However, the above numerical simulation methods were all derived on the basis of classical continuum mechanics, and classical theory has its limitations in terms of damage evolution and fracture failure. One issue is that classical theory is restricted by the continuity assumption, meaning that its equilibrium equation cannot be applied to discontinuous problems such as crack propagation, since partial differential derivatives do not exist in the equilibrium equation. Furthermore, the influence of crack failure cannot be directly reflected in the classical theoretical equilibrium equation, making it necessary to introduce external criteria or relationships to guide crack propagation. However, considering the complex propagation properties of cracks, which include oscillation, bifurcation, and turning, obtaining accurate fracture criteria or correlations is still a considerable challenge.

In view of the difficulties faced when classical theory was used to solve discontinuity problems, Silling [15] proposed the peridynamics (PD) theory, which is a new method for solving discontinuity problems such as crack propagation. PD theory describes the deformation of objects via an integral equation, where the impact of damage can be reflected by the bond disconnection in the equilibrium equation. Owing to the advantages of PD theory in solving discontinuity problems, this method is becoming increasingly common in the study of rail fatigue failure. For example, Ma et al. [16] characterized and verified the fatigue failure behavior of U75V rail materials under the composite loading mode on the basis of PD theory. Freimanis and Kaewunruen [17] studied the initiation and propagation of cracks during rail surface collapse. Ding et al. [18] studied the rolling contact fatigue crack propagation mechanism of laser-quenched rail materials. Ma et al. [19–21] established a PD model for simulating rail crack initiation and propagation and analyzed the rules of crack initiation and propagation in the U71Mn and U75V rails under the influence of various factors. Owing to the influence of nonlocal integral calculations, the computational efficiency of PD theory is lower than that of classical theories. To address this issue, Wang et al. [22, 23] proposed a parallel algorithm to improve the computational efficiency of fatigue analysis via a single-card graphics processing unit (GPU) and studied rail fatigue wear under thermal impact. Regarding the phenomenon of cavity defects in rails, Ma et al. [24] proposed a two-step prefabrication method for cavity defects and studied the fatigue failure rules for rails with different cavity defects.

At present, owing to the complexity of turnout structures, few studies have been carried out on rail crack propagation in turnouts on the basis of PD theory. Hamarat et al. [25] evaluated the fatigue failure of the point rail in a railway turnout via PD theory. Although a 3D model for the crack propagation of the point rail was established in this work, the simulation accuracy for the crack propagation path was poor because of the significant discrete distance between particles. In fact, if a smaller particle dispersion distance is used in the model, the computational efficiency of the 3D model decreases significantly. In this work, a 2.5-dimensional (2.5D) PD model for simulating crack propagation was proposed. Two types of additional constraints were applied to the 2D model, making its displacement field consistent with that of a 3D model; in this way, the 2D model can be used to simulate 3D crack propagation.

This work consists of the following sections: Section 2 introduces the ordinary state-based peridynamics (OSB PD) theory used for fatigue analysis. In Section 3, the bond fatigue failure condition is used to characterize the fatigue fracture performance of switch rail materials in a turnout. In Section 4, the PD model for rail crack propagation in a railway turnout is briefly introduced. To achieve the 3D simulation effect, two types of additional constraints and their derivation processes are introduced in Section 5. In Section 6, the accuracy of the 2.5D PD model for simulating rail crack propagation is verified on the basis of three aspects: model deformation, bond fatigue failure conditions of the material, and overall simulation accuracy.

2 OSB PD theory for fatigue analysis

2.1 OSB PD theory

The OSB PD theory is a PD method consisting of a force density vector, proposed by Silling in 2007 [26]. The relationship between the deformed state and the force state was proposed for the first time via PD theory, after which calculation methods for traditional mechanics theories could be introduced into PD methods. Compared with the bond type theory, this method can decouple the geometric deformation of the object, removing any restrictions on parameters such as the Poisson's ratio of the material. As shown in Fig. 1, the construction domain Ω of the continuum body is divided into finite particles, where any particle x interacts with any other particle x' in a certain range H; the radius δ of this range is known as the near-field dimension.

In Fig. 1, $\boldsymbol{u}$ and $\boldsymbol{u}'$ are the displacement vectors of the particles; if the vector of the relative displacement between two particles is defined as $\boldsymbol{\eta} = \boldsymbol{u}' - \boldsymbol{u}$ and the bond vector before deformation is defined as $\boldsymbol{\xi} = x' - x$, then the bond vector after deformation is defined as $\boldsymbol{\xi}+\boldsymbol{\eta}$. The particle equilibrium equation using OSB PD theory is given via Eq. (1):

$$\rho\ddot{\boldsymbol{u}}(x,t) = \int_H \left\{ \underline{\boldsymbol{T}}[x,t]\langle\boldsymbol{\xi}\rangle - \underline{\boldsymbol{T}}[x',t]\langle-\boldsymbol{\xi}\rangle \right\} \mathrm{d}H + \boldsymbol{b}(x,t) \quad (1)$$

where ρ is the material density; $\boldsymbol{b}$ is the external force density vector; $\underline{\boldsymbol{T}}[x, t]\langle\boldsymbol{\xi}\rangle$ and $\underline{\boldsymbol{T}}[x', t]\langle-\boldsymbol{\xi}\rangle$ are the force density vectors acting on the two particles, respectively. The calculation method is described in Refs. [26, 27].

2.2 Bond fatigue failure conditions

As shown in Eq. (2), a scalar function ψ is introduced into the particle equilibrium equation to reflect the impact of fatigue failure, such as cracks [28].

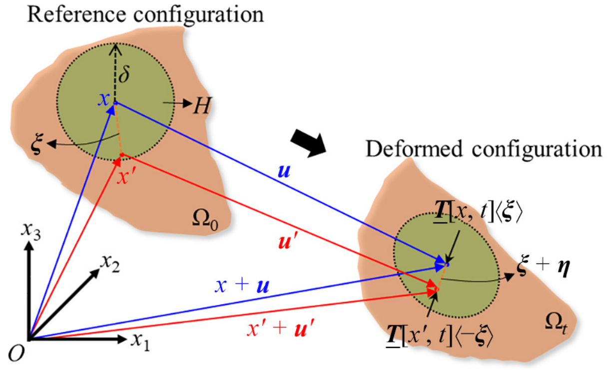

Fig. 1 Schematic diagram of particle interactions [21].

$$\rho \ddot{\boldsymbol{u}}(x,t) = \int_H \psi[\boldsymbol{\xi},t]\{\underline{\boldsymbol{T}}[x,t]\langle\boldsymbol{\xi}\rangle - \underline{\boldsymbol{T}}[x',t]\langle-\boldsymbol{\xi}\rangle\}\,\mathrm{d}H + \boldsymbol{b}(x,t) \tag{2}$$

The scalar function $\psi = 1$ before the bond breaks and $\psi = 0$ when it breaks. In terms of steel rails and other ductile materials, Silling and Askari [29] proposed a suitable fatigue analysis method. They assigned each bond an initial residual fatigue life λ of 1, with λ decreasing as the number of load cycles, N, increased. When the residual fatigue life of the bond decreases to 0, the bond breaks. The reduction rate of the remaining fatigue life of the bond can then be calculated via Eq. (3):

$$\begin{cases} \mathrm{d}\lambda/\mathrm{d}N = -A\varepsilon^m \\ \varepsilon = |s_{\max} - s_{\min}| \end{cases} \tag{3}$$

where A and m are undetermined constants related to the bond fatigue failure condition, and their values depend on the fatigue fracture properties of the materials. ε is the bond stretch amplitude of a single loading process, while $s_{\max}$ and $s_{\min}$ are the maximum and minimum bond stretches, respectively, during a single loading process.

In PD theory, the local damage coefficient of a particle is often used to characterize the propagation path of a crack. This coefficient is the ratio of the number of broken bonds to the total number of bonds in the near-field range of the particle.

3 Bond failure conditions for turnout rail materials

3.1 Fatigue crack propagation rate experiment

The U71Mn turnout rail material was selected for the fatigue crack propagation rate experiment. The chemical compositions and mechanical and fracture mechanical properties of the U71Mn rail material are shown in Tables 1 and 2 [30, 31], respectively.

In Table 2, $\sigma_{0.2}$ and σ_b represent the 0.2% offset yield strength and tensile strength, respectively; Δs represents elongatio; ψ is the reduction in the cross section; K_{IC} is the plane-strain fracture toughness.

Table 1 Chemical compositions of U71Mn rail material (wt%) [30]

Rail material	C	Si	Mn	P	S	V
U71Mn	0.710	0.250	1.410	≤ 0.030	≤ 0.030	0.040

Table 2 Mechanical and fracture mechanical properties of U71Mn rail material [30, 31]

Rail material	Mechanical property			Fracture mechanics property	
	$\sigma_{0.2}$ (MPa)	σ_b (MPa)	Δs (%)	K_{IC} (MPa·m$^{1/2}$)	ψ (%)
U71Mn	552.0	964.0	13.0	45.2	39.0

According to the position and direction shown in Fig. 2, a number of compact tensile shear samples were taken from the U71Mn turnout rail for use as test objects. In the figure, x, y, and z are the longitudinal, lateral, and vertical directions of the railway line, respectively; W is the sample width; B is the sample thickness; q is the crack length of the sample.

As shown in Fig. 3, the sample was installed on an MTS809 fatigue testing machine via a clevis, after which a fatigue crack propagation rate experiment was conducted for the samples under single type I loading. The loading frequency f = 10 Hz and load ratio R = 0.1 were set, with the maximum loads $P_{\max}$ of 13 and 15 kN, respectively. An experiment with a maximum load of 13 kN was used to determine the bond fatigue failure condition of the turnout rail material, whereas an experiment with a maximum load of 15 kN was used to verify the bond fatigue failure condition.

A high-precision industrial camera (CCD camera) was used to observe and record the crack propagation process during the experiment.

During the fatigue crack propagation rate experiment of the above material, it was possible to determine how the crack length of the sample changed with the number of loading cycles (Fig. 4).

3.2 PD model for specimen loading

Based on the size of the compact tensile shear sample, a PD model for sample loading was established in the Cartesian plane coordinate system Oxy, as shown in Fig. 5 [32]. The discrete size of the model was 0.5 mm. Owing to the sample batches and testing errors, there are some differences in the elastic modulus and Poisson's ratio values of the U71Mn rail materials used in different studies. According to Refs. [33, 34], the elastic modulus of the U71Mn rail material ranges from approximately 204 to 210 GPa, and the Poisson's ratio is typically 0.3. Therefore, the elastic modulus and Poisson's ratio of the U71Mn rail material

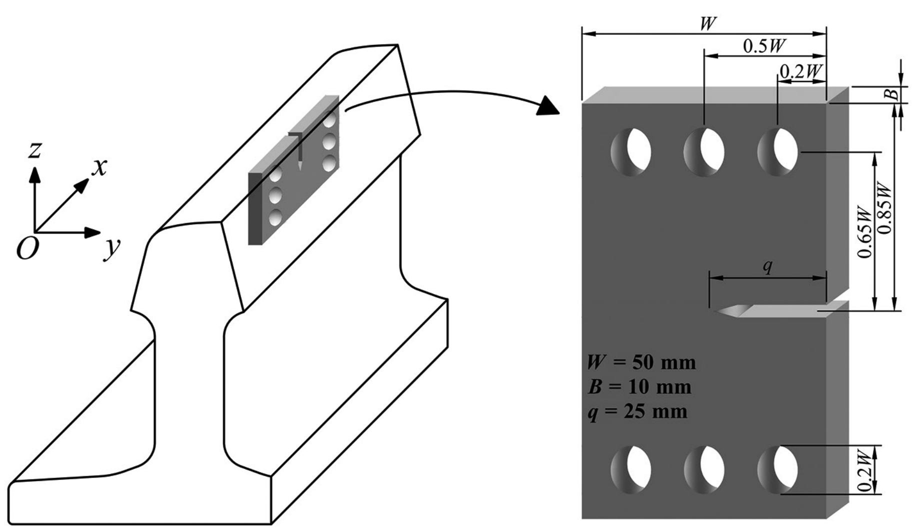

Fig. 2 Sampling position and dimensions of compact tensile shear samples.

used in the PD model constructed in this work are 206 GPa and 0.3, respectively.

In the model shown in Fig. 5, total external loads of $P/2$ were applied to the particles in four circular hole regions, where P was the load applied by the fatigue testing machine. The displacement boundary condition $U_x = 0$ was applied separately to the particles in the upper and lower left corners of the model, while $U_y = 0$ was applied to the center left particle of the model [35].

3.3 Bond failure conditions

For compact tensile shear samples, the change rate ΔK of the stress intensity factor at the crack tip is calculated via Eq. (4) [36]:

$$\Delta K = \frac{P}{WB}\sqrt{\pi q}\frac{\cos\alpha}{1-q/W} \times \sqrt{\frac{0.26+2.65\,[q/(W-q)]}{1+0.55\,[q/(W-q)]-0.08[q/(W-q)]^2}} \tag{4}$$

where P is the load imposed by the fatigue testing machine; α is the angle between the loading force direction and the normal direction of the crack plane ($\alpha = 0$ in this work); q is the crack length; W and B are the size parameters of the sample. The parameters related to the sample sizes are shown in Fig. 2.

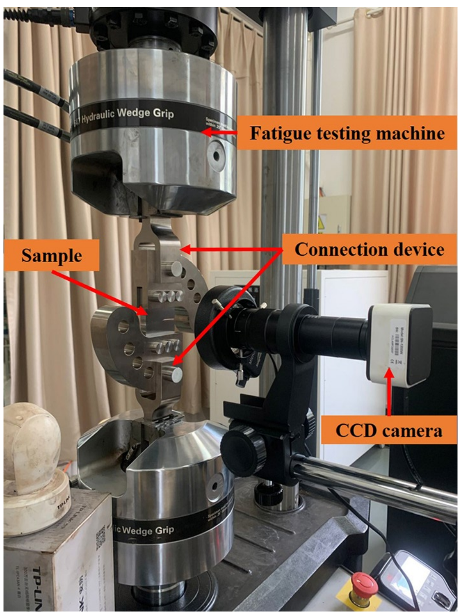

Fig. 3 Fatigue crack propagation rate experiment.

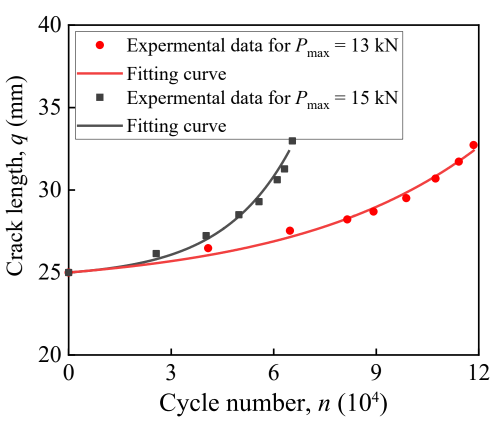

Fig. 4 Crack length of sample vs. number of loading cycles ($R = 0.1$).

Using the experimental results for P_{max} = 13 kN, as shown in Fig. 4, the relationship between the crack propagation rate and the variation in the stress intensity factor was calculated (Fig. 6).

The Paris law was used to fit the experimental data for the crack propagation of the material, with a fitting formula obtained as Eq. (5):

$$dq/dN = 2.3492e - 9\Delta K^{3.07053} \tag{5}$$

The m value in the bond fatigue failure condition of the turnout rail material was determined to be 3.07053 using the method described in Ref. [29] for the calculation of undetermined constants for the bond fatigue failure condition. It was assumed that $A_{trial} = 3\times10^4$; then, under the conditions of a maximum load P_{max} = 13 kN and load ratio R = 0.1, the simulation results for crack propagation in a sample could be obtained from the PD model for sample loading established in Section 3.2, as shown in Fig. 7.

On the basis of the simulation results shown in Fig. 7, the relationship between the crack propagation rate and the change in the stress intensity factor of the sample can be calculated (Fig. 6). As shown in Fig. 6, there is a significant difference between the PD simulation results and the experimental results. The reason for this discrepancy is that the trail value A_{trail} was assigned to A, which is not a correct value. This results in a significant difference between the simulation results and the experimental results. This

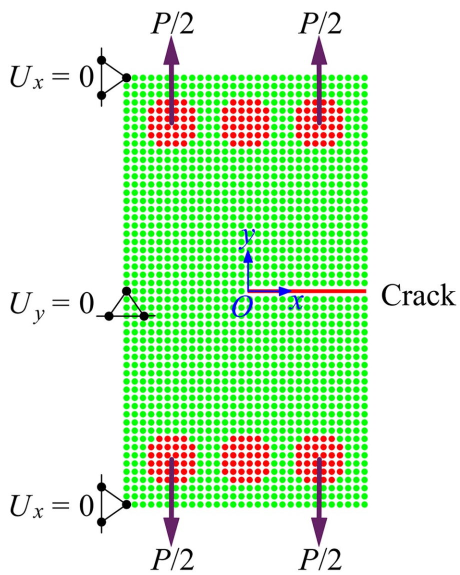

Fig. 5 Schematic diagram of PD model for sample loading.

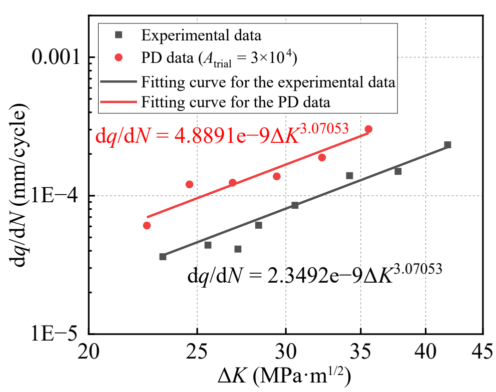

Fig. 6 Relationship between crack propagation rate and variation amplitude of stress intensity factor.

difference will be used to modify the A_{trail} and obtain the correct A value in Eq. (3).

The Paris law was once more used to fit the crack propagation simulation data, with the fitting formula obtained via Eq. (6):

$$dq/dN = 4.8891\,e - 9\Delta K^{3.0705} \tag{6}$$

Based on Eqs. (5) and (6), the key parameter A for the bond fatigue failure condition of the turnout rail material was modified to Eq. (7):

$$A = A_{trial} \times \frac{2.3492e - 9\Delta K^{3.07053}}{4.8891e - 9\Delta K^{3.07053}} = 1.4415 \times 10^4 \tag{7}$$

Based on the undetermined constants A and m for the bond fatigue failure condition derived in this section, the bond fatigue failure condition of the turnout rail material can be obtained via Eq. (8):

$$d\lambda/dN = -1.4415 \times 10^4 \cdot \varepsilon^{3.07053} \tag{8}$$

4 PD model for rail crack propagation in railway turnouts

4.1 Model overview

In this work, the switch rail in a railway turnout was taken as the test object, with a PD model for crack propagation established in the $Oxyz$ coordinate system, as shown in Fig. 8. In this figure, q_0 is the initial crack length; β is the angle between the initial crack and the horizontal plane; x, y, and z are the longitudinal, lateral, and vertical directions of the railway line, respectively.

To better simulate crack propagation, the discrete particle size of the model should be as small as possible. However, if the entire section is discretized at a smaller size, then the computational efficiency will be significantly reduced. Therefore, to balance the calculation accuracy and efficiency, discrete dimensions of 0.2 mm × 0.2 mm were used in the area of concern for crack propagation (the red box shown in Fig. 8), whereas dimensions of 0.4, 0.8, and 1.6 mm were used in other areas. In traditional PD theory, ghost forces occur when different discrete dimensions are used. To counteract this, the dual PD method [37] was used in this work to solve the issue of inconsistent discrete dimensions for particles. The method described in Ref. [38] could also be used to solve the problem of multiple discrete dimensions.

The particles on both sides of the cracks in the model can penetrate each other during the crack closing process (Fig. 9). To avoid this unreasonable phenomenon of mutual penetration, a short-range repulsive force was applied to the crack particles to simulate the contact between cracks during the closing process, as described in Refs. [21, 39].

4.2 Displacement boundary conditions

When a train passes through a turnout, the switch rail is attached to and locked onto the stock rail; as a result, a lateral displacement constraint of $U_y = 0$ is applied in the model on the close contact face between the switch rail and the stock rail. In addition, for the

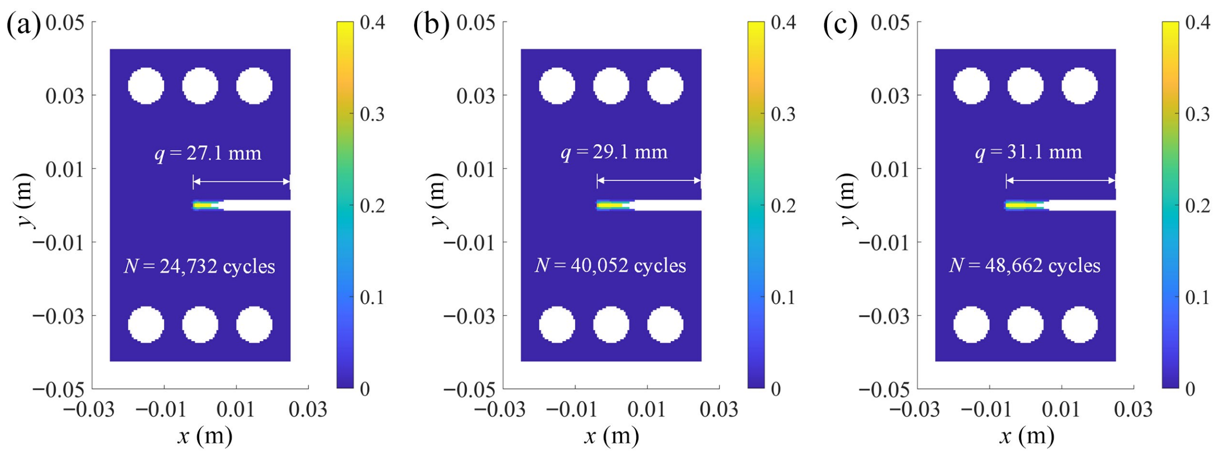

Fig. 7 Simulation results for crack propagation via PD model (P_{max} = 13 kN).

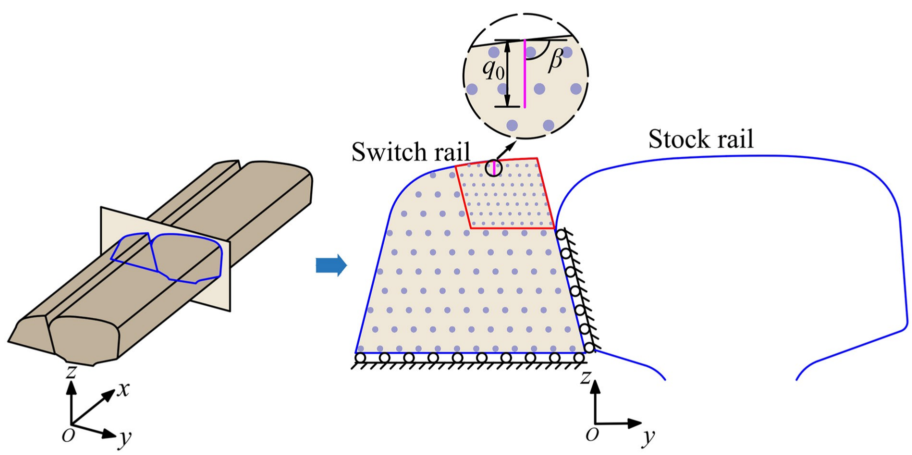

Fig. 8 Diagram of PD model for switch rail crack propagation.

model used in this work, a part of the switch rail was truncated. Since there was no obvious displacement between the truncated switch rail and the body, a vertical displacement constraint of U_z = 0 was applied to the bottom of the switch rail.

4.3 Load boundary conditions

The external load borne by the switch rail comes from the cyclic rolling contact of the wheel. As shown in Fig. 10, based on the relative positional relationship between the wheel and switch rail within the model, the real-time integration method was used to calculate the dynamic load of the wheel applied in the model area. This simulated the change in load during wheel rolling. In the figure, l is the 2D model thickness.

(1) Normal contact

According to Hertzian contact theory [40], the contact spot between the wheel and rail is elliptic. The relative positional relationship between the elliptic contact spot and the switch rail model during the wheel rolling process is shown in Fig. 11.

As shown in Fig. 11, assuming that the coordinates of the elliptic contact spot center O_1 at any position are (x_t, y_t), the equation for the elliptic contact spot is defined as Eq. (9):

$$\frac{(x-x_t)^2}{a^2}+\frac{(y-y_t)^2}{b^2}=1 \tag{9}$$

where a and b are the semimajor and semiminor axes of the contact spot, respectively. When the contact spot boundary intersects with the left-hand boundary of the model, the coordinates of the two points of intersection y_1 and y_2 are shown in Eq. (10).

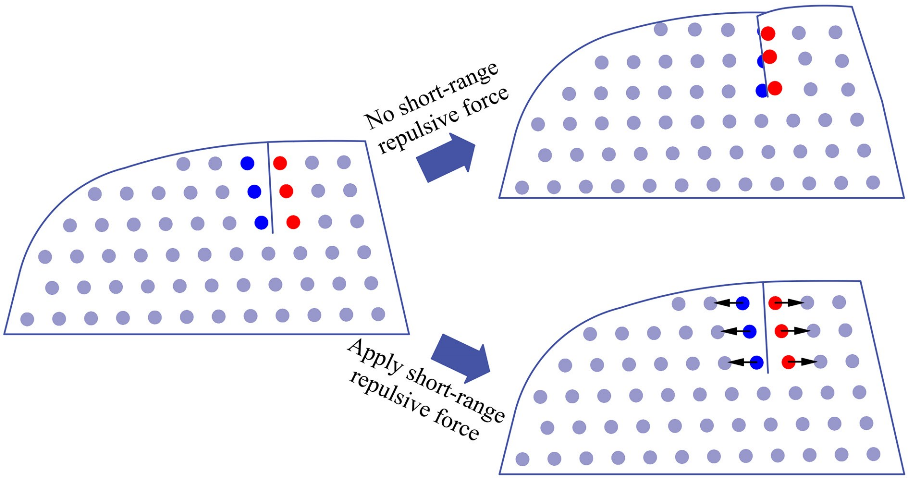

Fig. 9 Contact simulation during crack closing process.

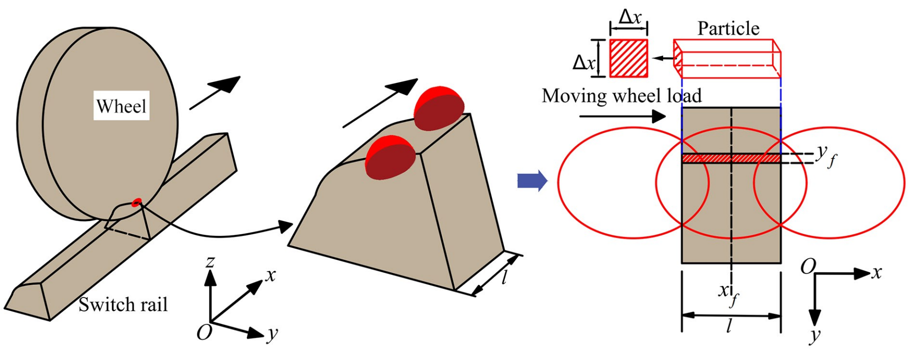

Fig. 10 Diagram of wheel rolling contact action.

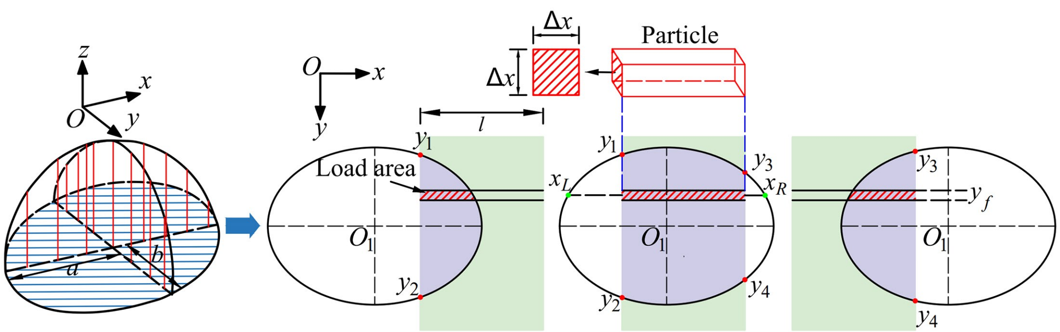

Fig. 11 Diagram of relative position between contact spot and model.

$$\begin{cases} y_1 = y_t - b\sqrt{1 - \dfrac{(x_f - l/2 - x_t)^2}{a^2}}, \\ \qquad x_t \in [x_f - l/2 - a, x_f - l/2 + a] \\ y_2 = y_t + b\sqrt{1 - \dfrac{(x_f - l/2 - x_t)^2}{a^2}}, \\ \qquad x_t \in [x_f - l/2 - a, x_f - l/2 + a] \end{cases} \tag{10}$$

where x_f is the x-axis coordinate of the particle center and l is the thickness of the switch rail model along the x-axis. Similarly, when the contact spot boundary intersects with the right-hand boundary of the model, the coordinates of the two points of intersection, y_3 and y_4, are shown in Eq. (11).

$$\begin{cases} y_3 = y_t - b\sqrt{1 - \dfrac{(x_f + l/2 - x_t)^2}{a^2}}, \\ \qquad x_t \in [x_f + l/2 - a, x_f + l/2 + a] \\ y_4 = y_t + b\sqrt{1 - \dfrac{(x_f + l/2 - x_t)^2}{a^2}}, \\ \qquad x_t \in [x_f + l/2 - a, x_f + l/2 + a] \end{cases} \tag{11}$$

Equation (12) is then used to determine whether any particle bears the wheel load, that is, whether the particle area overlaps with the contact spot area.

$$\begin{cases} y_1 < y_f < y_2, x_t \in [x_f - l/2 - a, x_f - l/2] \\ y_t - b < y_f < y_t + b, x_t \in [x_f - l/2, x_f + l/2] \\ y_3 < y_f < y_4, x_t \in [x_f + l/2, x_f + l/2 + a] \end{cases} \tag{12}$$

where y_f is the y-axis coordinate of any particle. For particles subjected to wheel loading, their extension lines along the x-axis intersect with the boundary of the contact spot. The x-axis coordinates for the left intersection x_{L} and right intersection x_{R} are calculated via Eq. (13):

$$\begin{cases} x_{\mathrm{L}} = -a\sqrt{1 - \dfrac{(y_f - y_t)^2}{b^2}} + x_t \\ x_{\mathrm{R}} = +a\sqrt{1 - \dfrac{(y_f - y_t)^2}{b^2}} + x_t \end{cases} \tag{13}$$

The normal wheel–rail contact stress $\sigma_z(x, y)$ of a particle bearing a wheel load at any position (x, y) is given via Eq. (14):

$$\begin{cases} \sigma_z(x,y) = \sigma_{\max}\sqrt{1 - \dfrac{(x - x_t)^2}{a^2} - \dfrac{(y - y_t)^2}{b^2}} \\ \sigma_{\max} = \dfrac{3P_z}{2\pi ab} \end{cases} \tag{14}$$

where P_z is the total normal force of the wheel applied to the rail. According to the integral calculation result for a region where any particle bears the wheel load, the normal contact action for any particle is described by Eq. (15):

$$F_{z,f} = \int_{\max(x_f - \frac{l}{2}, x_{\mathrm{L}})}^{\min(x_f + \frac{l}{2}, x_{\mathrm{R}})} \int_{y_f - \frac{\Delta x}{2}}^{y_f + \frac{\Delta x}{2}} \sigma_z(x,y)\mathrm{d}x\mathrm{d}y \tag{15}$$

where Δx is the discrete distance between particles.

(2) Tangential contact

In most cases, the wheel–rail contact is maintained in the creep state; that is, both an adhesive area (A_k) and a sliding area (S_k) exist in the contact spot at the same time, and only in extreme cases will it be in a single sliding state. As shown in Fig. 12, the Johnson–Vermeulen 3D rolling contact theory [41] was adopted in this work, while the adhesive area in the wheel–rail contact spot was assumed to be elliptical.

The relationship between the elliptical sizes in the adhesive area and the contact spot sizes is defined as Eq. (16):

$$\left(\frac{a_{\mathrm{A}}}{a}\right)^3 = \left(\frac{b_{\mathrm{A}}}{b}\right)^3 = 1 - \frac{P_\tau}{\mu P_z} \tag{16}$$

where a_{A} and b_{A} are the semimajor and semiminor axes of the ellipse in the adhesive area, respectively; μ is the friction coefficient; P_τ is the total tangential force at the contact spot. Since the model established in this work is in the Oyz plane (Fig. 8), only tangential contact changes caused by the lateral creep rate, ξ_y are considered. The total tangential contact force P_τ is calculated via Eq. (17).

$$P_\tau = \mu P_z \begin{cases} \left[\left(1 - \dfrac{\xi}{3}\right)^3 - 1\right], & |\xi| < 3 \\ 1, & |\xi| \geqslant 3 \end{cases} \tag{17}$$

where ξ is the normalized creep rate and can be calculated via Eq. (18):

$$\xi = \frac{\pi abG\xi_y}{\mu P_z \psi_1} \tag{18}$$

where G is the shear modulus of the material; ξ_y is the lateral creep rate; ψ_1 can be calculated via Eq. (19):

$$\psi_1 = \begin{cases} B - v\left(\dfrac{a^2}{b^2}\right)C, \ a \leqslant b \\ \dfrac{(D - vC)b}{a}, \quad a > b \end{cases} \tag{19}$$

where v is Poisson's ratio and B, D, and C are complete elliptic integrals. These parameters can be calculated via Eq. (20):

$$\begin{cases} B = \displaystyle\int_0^{\frac{\pi}{2}} \frac{\cos^2\theta}{\sqrt{1 - k^2\sin^2\theta}}\mathrm{d}\theta \\ D = \displaystyle\int_0^{\frac{\pi}{2}} \frac{\sin^2\theta}{\sqrt{1 - k^2\sin^2\theta}}\mathrm{d}\theta \\ C = \displaystyle\int_0^{\frac{\pi}{2}} \frac{\cos^2\theta\sin^2\theta}{\sqrt{1 - k^2\sin^2\theta}}\mathrm{d}\theta \end{cases} \tag{20}$$

The value of k^2 in this equation is shown in Eq. (21):

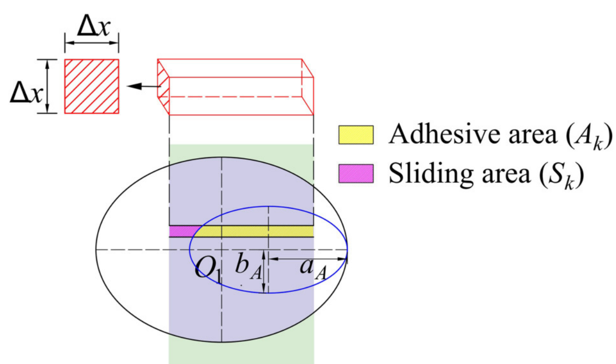

Fig. 12 Diagram of adhesive area and sliding area at elliptical contact spot.

清華大学出版社 Tsinghua University Press | SciOpen

$$k^2 = \begin{cases} 1 - \dfrac{a^2}{b^2}, & a \leqslant b \\ 1 - \dfrac{b^2}{a^2}, & a > b \end{cases} \tag{21}$$

The total tangential contact force P_τ can be calculated via Eqs. (17)–(21), whereas the size of the ellipse in the adhesive area can be obtained via Eq. (16); the wheel–rail tangential contact stress at any position (x, y) can be calculated via Eq. (22):

$$\tau_y(x,y) = \begin{cases} \mu\sigma_z(x,y), \\ \qquad (x,y) \in \{S_k\} \\ \mu\sigma_z(x,y) - \mu\sigma_{\max}\dfrac{a_{\mathrm{A}}}{a} \\ \cdot\sqrt{1 - \dfrac{(x - x_t - a + a_{\mathrm{A}})^2}{a_{\mathrm{A}}^2} - \dfrac{(y - y_t)^2}{b_{\mathrm{A}}^2}}, \\ \qquad (x,y) \in \{A_k\} \end{cases} \tag{22}$$

where $\sigma_z(x, y)$ is the normal contact stress at the corresponding position and $\sigma_{\max}$ is the maximum normal wheel–rail contact stress at the contact spot. By calculating the integral of the region where any particle bears the wheel load, the tangential contact action of any particle is given by Eq. (23):

$$F_{\tau,f} = \int_{\max(x_f - \frac{l}{2}, x_{\mathrm{L}})}^{\min(x_f + \frac{l}{2}, x_{\mathrm{R}})} \int_{y_f - \frac{\Delta x}{2}}^{y_f + \frac{\Delta x}{2}} \tau_y(x,y)\mathrm{d}x\mathrm{d}y \tag{23}$$

5 2.5D additional constraints of PD model

5.1 Additional constraints for crack opening

As shown in Fig. 13, in a 3D situation, the substances at both ends of a longitudinal crack along the railway line restrict the crack opening. The smaller the longitudinal crack width b_0 is, the greater the constraint on crack opening. In contrast, the larger the longitudinal crack width b_0 is, the smaller the constraint.

However, the interactions between the particles on both sides of the crack are lost in the plane model. Therefore, when the crack opens, there will be a large relative displacement between these particles; this displacement is quite different from the actual opening state of 3D cracks. Since a discontinuous space (crack) will be formed after the bond breaks, a constraint with stiffness k_1 was applied between particles without interactions (Fig. 14) to simulate the constraining effect when cracks open in a 3D structure.

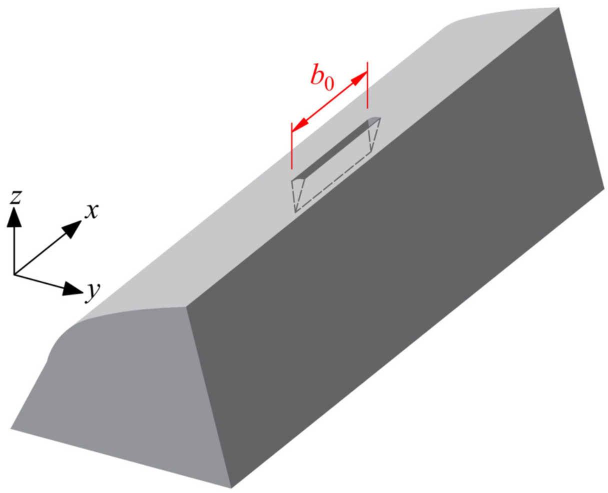

Fig. 13 Schematic diagram of a crack in a 3D turnout switch rail.

As shown in Fig. 15, a beam structure with fixed ends can be used to study the relative relationship during 3D crack opening. Under the action of two loads, each with a value of $F_0/2$, a 3D crack changes from its initial closed state to an open state. The maximum crack opening displacement is Δl_0, which can be calculated via Eq. (24):

$$\begin{cases} \Delta l_0 = \dfrac{F_0 b_0^3}{192EI} \\ I = \dfrac{(\Delta x)^4}{12} \end{cases} \tag{24}$$

where b_0 is the longitudinal width of the crack, EI is the flexural stiffness of the particle cross section, and Δx is the discrete distance between particles.

To simulate the interaction between any two particles during crack opening in the plane model, the interaction between them is simplified as a constraint spring with a stiffness of k_1. Under the action of two loads $F_0/2$, the two particles will produce the same relative displacement Δl_0, as shown in Eq. (24). Therefore, the equivalent constraint stiffness k_1 can be calculated via Eq. (25):

$$k_1 = \frac{F_0}{\Delta l_0} = \frac{192EI}{b_0^3} \tag{25}$$

The interactive force $\boldsymbol{f}_{cf1}$ is applied to particles that meet the following two conditions: (i) the bonds between the particles break; (ii) the distance between the particles $\|\boldsymbol{\xi}+\boldsymbol{\eta}\|$, which is greater than the initial distance $\|\boldsymbol{\xi}\|$ (meaning that the crack is in an open

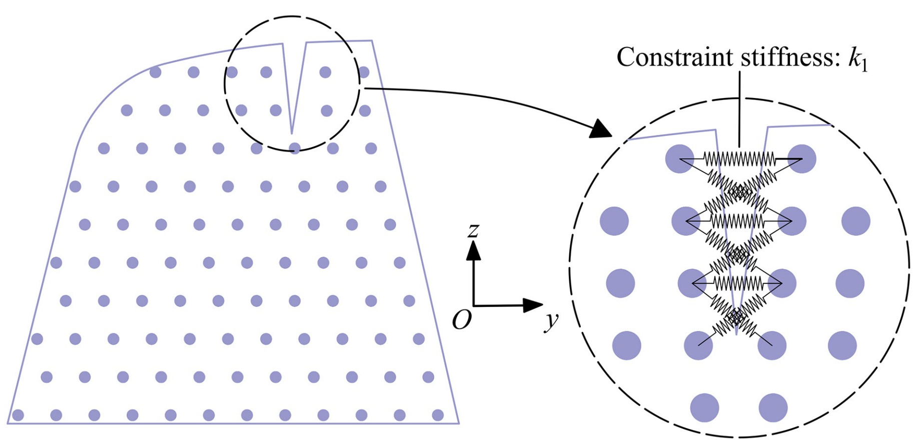

Fig. 14 Schematic diagram of additional constraints between particles during crack opening.

state at this time), after deformation. The interactive force $\boldsymbol{f}_{cf1}$ can be calculated via Eq. (26):

$$\boldsymbol{f}_{cf1} = \frac{\boldsymbol{\xi}+\boldsymbol{\eta}}{\|\boldsymbol{\xi}+\boldsymbol{\eta}\|}\max\{0,\ k_1(\|\boldsymbol{\xi}+\boldsymbol{\eta}\| - \|\boldsymbol{\xi}\|)\} \tag{26}$$

5.2 Additional constraints on the cross section

Owing to the limitation of computational efficiency, it was necessary to truncate a section of the switch rail with a thickness of t_0 to construct a 3D model. For the two cross sections of this 3D model, fixed constraints are usually used as displacement boundary conditions, which constrain the deformation of the plane model. The larger the truncation thickness t_0 is, the smaller the constraint applied to the 2D model. In contrast, a smaller truncation thickness leads to a greater constraint.

To simulate the effect of this constraint on a cross section applied on a plane model, a constraint with stiffness k_2 is applied to all the particles in the plane model (Fig. 16).

As shown in Fig. 17, the maximum shear displacement δ_0 is generated at the center section of the structure under a load F_0.

Since the deformation of a structure under load is far smaller than its original size (satisfying the small deformation hypothesis), the maximum shear displacement δ_0 can be calculated via Eq. (27):

$$\begin{cases} \delta_0 = \dfrac{t_0}{2}\cdot\tan\theta_0 \\ \tan\theta_0 \approx \theta_0 = \gamma \end{cases} \tag{27}$$

where γ is the shear strain, which can be calculated via Eq. (28):

$$\begin{cases} \gamma = \dfrac{\tau_0}{G} = \dfrac{\dfrac{F_0/2}{A_s}}{G} \\ G = \dfrac{E}{2(1+\nu)} \end{cases} \tag{28}$$

where τ_0 is the shear stress; G and E are the shear modulus and elastic modulus of the material, respectively; A_s is the sectional area.

To simulate the constraint effect of the truncation boundary on the particle displacement in a plane model, a constraint with a stiffness of k_2 is applied to every particle. Under the action of a load F_0, the particle generates the same maximum displacement δ_0 as that described in Eq. (27). Therefore, the equivalent constraint stiffness k_2 can be calculated via Eq. (29):

$$k_2 = \frac{F_0}{\delta_0} = \frac{2EA_s}{t_0(1+\nu)} \tag{29}$$

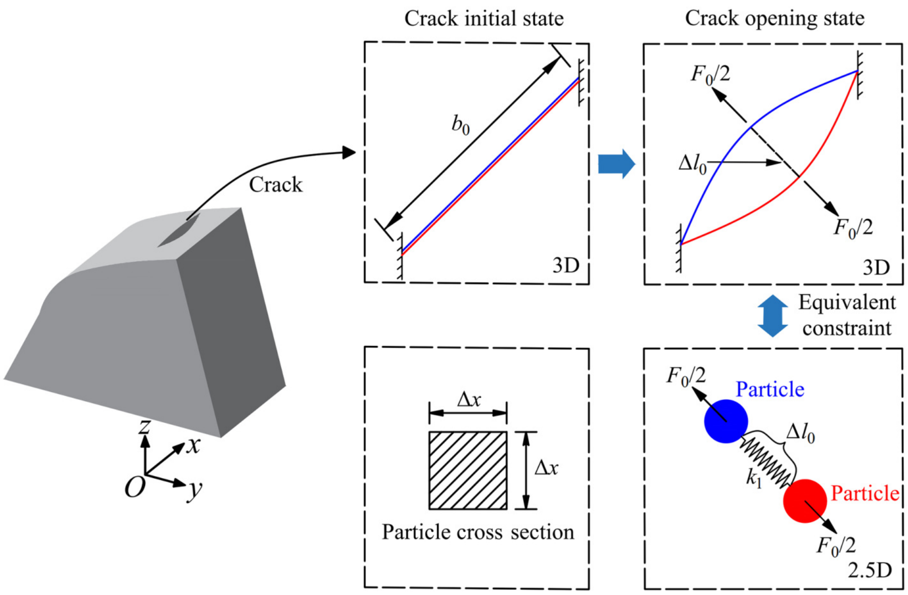

Fig. 15 Derivation diagram for constraint stiffness k_1.

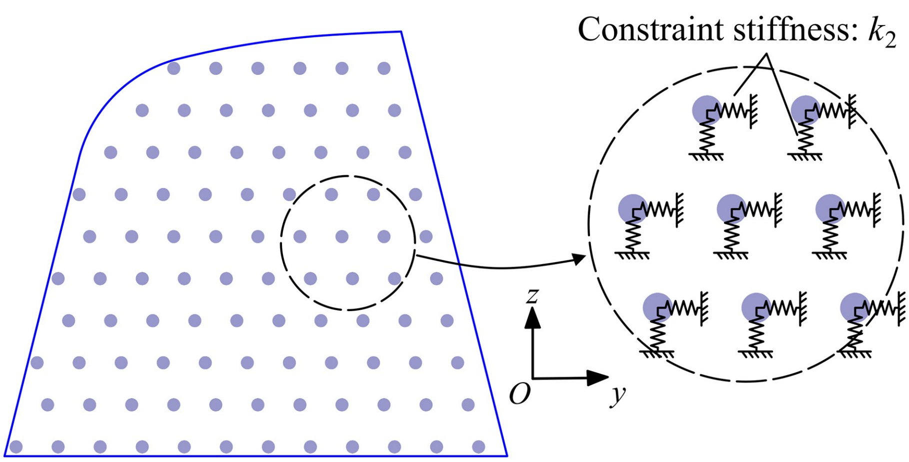

Fig. 16 Schematic diagram of additional constraints on particles.

清華大学出版社 Tsinghua University Press | SciOpen

The binding force $\boldsymbol{f}_{cf2}$ on any particle in the plane model can be expressed via Eq. (30):

$$\boldsymbol{f}_{cf2} = -k_2 \cdot \boldsymbol{u} \tag{30}$$

where $\boldsymbol{u}$ is the displacement vector of the particle.

6 Model verification

In this section, the 2.5D-PD model for rail crack propagation in a railway turnout established in this work is verified from three aspects: structural deformation, fatigue fracture performance, and overall crack propagation simulation accuracy.

6.1 Model deformation verification

A structural deformation model for a switch rail with cracks was established for this work (Fig. 18) via the finite element method (FEM). ANSYS software was used to establish the 3D-FEM model, and 8-node solid45 elements were used for mesh discretization of the structure. The mesh discretization was carried out by combining the free meshing and mapped meshing methods, and the grid size was 0.5 mm. The elastic modulus and Poisson's ratio of the material used in the FEM model were 206 GPa and 0.3, respectively. The model is solved via the static analysis module.

A fixed constraint was applied to the two cross sections at the front and back of the model (along the x-axis direction), a vertical constraint was applied to the bottom in the z-axis direction, and a lateral constraint was applied to the area where the model was attached to the stock rail in the y-axis direction. Since the FEM itself is a 3D model, there is no need to apply the k_1 and k_2 constraints, which are described in Section 5, to the FEM. The load conditions for the model were consistent with those of the PD model: total vertical load of 77.4 kN, wheels and rails in the single sliding contact state, tangential force direction in the positive direction of the y-axis, friction coefficient of 0.3, load center 3 mm away from the apex of the working edge of the switch rail, semimajor axis a of the contact spot of 6.92 mm and semiminor axis b of 2.63 mm.

The Fortran language was used to compile the calculation program of the 2.5D-PD model. A total of 5,824 particles with volume and mass information were used for meshless discretization of the rail structure. The spacing between particles is 0.5 mm. The material parameters used in the 2.5D-PD model are consistent with those used in the 3D-FEM model. The adaptive dynamic relaxation method [42] was used to conduct the static analysis. Unlike in the 3D-FEM model, the k_1 and k_2 constraints described in Section 5 were applied to the 2.5D-PD model.

To verify the accuracy of the two types of additional constraints described in Section 5, a comparative analysis was performed on three cases of structural deformation simulation: (i) b_0 = 3 mm and t_0 = 30 mm; (ii) b_0 = 5 mm and t_0 = 30 mm; (iii) b_0 = 5 mm and t_0 = 25 mm. The starting point of the crack was set at 8 mm from the apex of the working edge of the switch rail, lying parallel to the non-working edge of the switch rail, with a crack length of 5 mm. A 2.5D-PD model and a 3D-FEM model were used to simulate the deformation of the switch rail, and the simulation results are shown in Figs. 19–21. The displacements in the figures are amplified 50-fold for easier understanding.

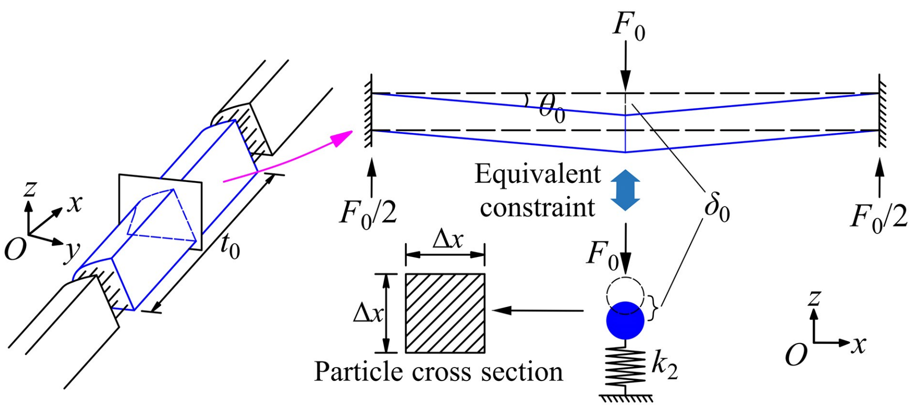

Fig. 17 Derivation diagram of constraint stiffness k_2.

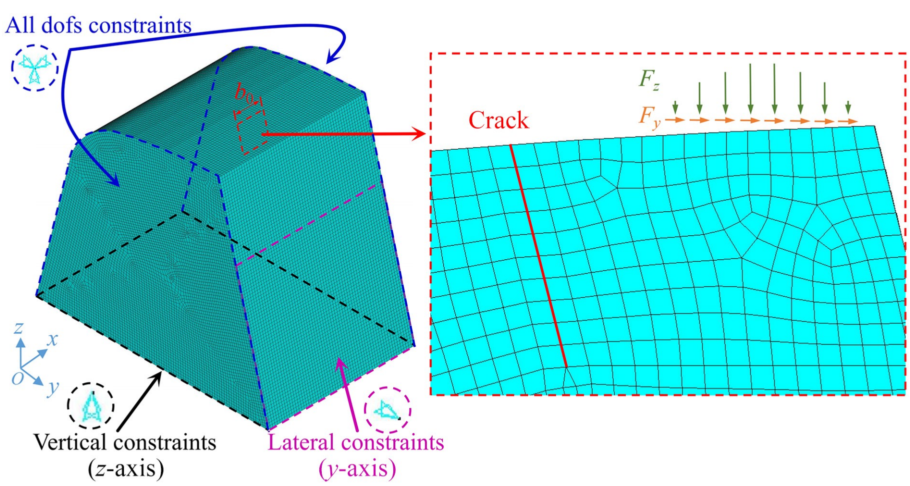

Fig. 18 Diagram of FEM model for simulating structural deformation of switch rail.

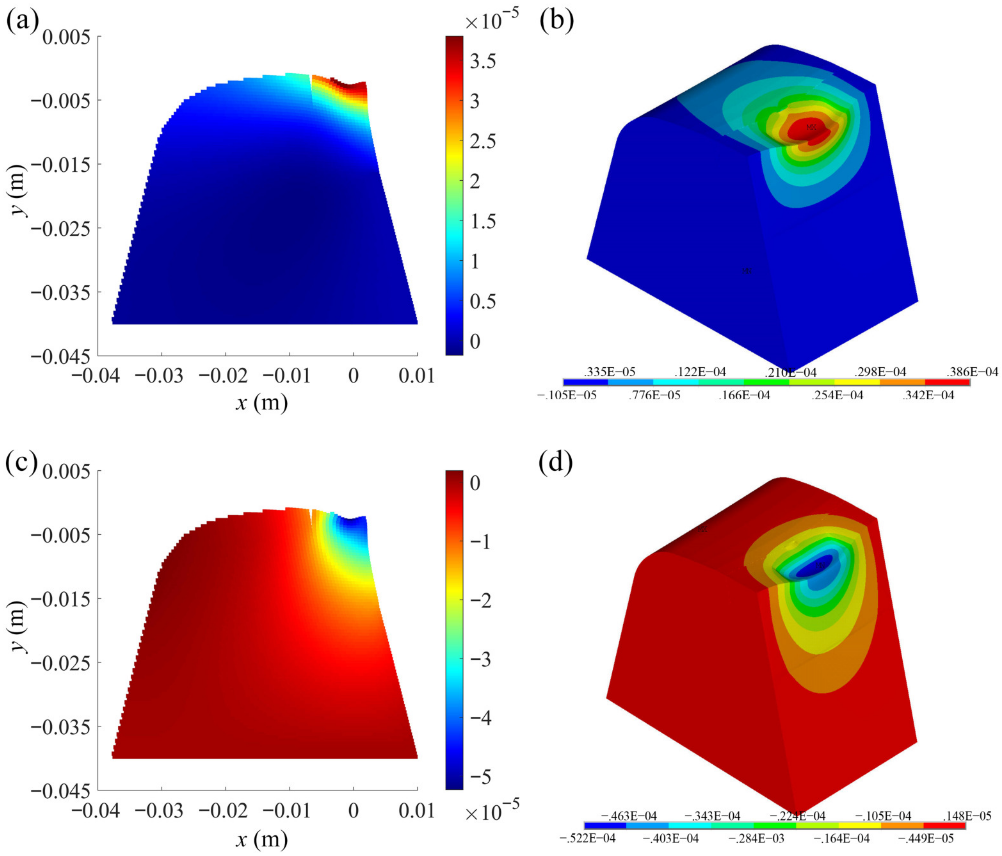

Fig. 19 Displacement calculation results for b_0 = 3 mm and t_0 = 30 mm (unit: m): (a) lateral displacement of 2.5D-PD model, (b) lateral displacement of 3D-FEM model, (c) vertical displacement of 2.5D-PD model, and (d) vertical displacement of 3D-FEM model.

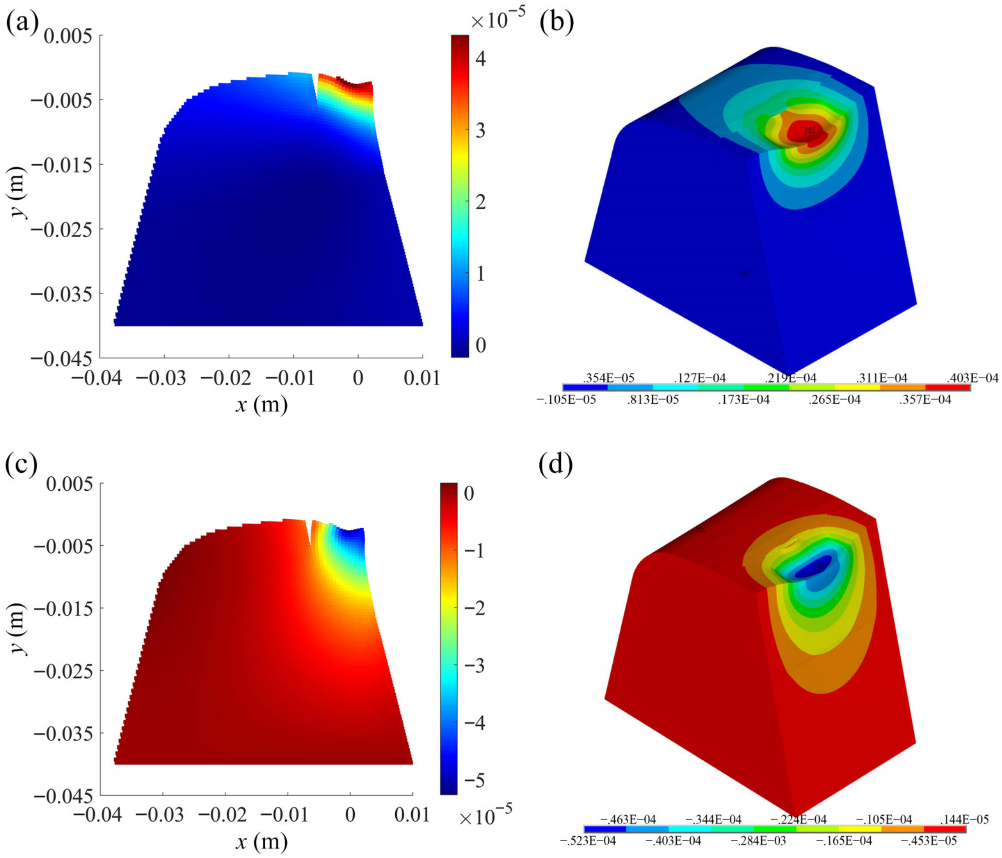

Fig. 20 Displacement results for b_0 = 5 mm and t_0 = 30 mm (unit: m): (a) lateral displacement of 2.5D-PD model, (b) lateral displacement of 3D-FEM model, (c) vertical displacement of 2.5D-PD model, and (d) vertical displacement of 3D-FEM model.

The maximum displacement calculations extracted for the 2.5D-PD and 3D-FEM models are shown in Table 3. Errors are calculated based on the 3D-FEM model.

As shown in Table 3, compared with those of the 3D-FEM model, the maximum lateral displacement and vertical displacement calculation errors for the 2.5D-PD model are within 8% and 1%, respectively, thus verifying the accuracy of the 2.5D-PD model established in this work for calculating the overall deformation of a switch rail.

If the two types of constraints described in Section 5 are not applied, then the lateral and vertical displacement calculations of the 2D-PD model are as shown in Fig. 22. The displacements in Fig. 22 are amplified 50-fold for easier understanding.

As shown in Table 1 and Fig. 22, the displacement calculations for the 2D-PD model without constraints are significantly different from those for the 3D-FEM model. To further compare the crack opening simulations for the three different models, the crack opening states simulated based on the 3D-FEM, 2.5D-PD, and 2D-PD models were separately extracted (Fig. 23). The displacements in Fig. 23 are amplified 20-fold for easier understanding.

As shown in Fig. 23, compared with that of the 2D-PD model, the crack opening state of the 2.5D-PD model established in this work is very close to that of the 3D-FEM model, which verifies the accuracy of the 2.5D-PD model established in this work for simulating the crack opening state.

In addition, to compare the computational efficiency between the 2.5D-PD model and the 3D-FEM model, the computation time data of the two models under the same computer hardware conditions are listed in Table 4. All the numerical simulations use one 3.0 GHz Intel Core processor with 24 cores.

As shown in Table 4, compared with the 3D-FEM model, the proposed 2.5D-PD model has greater computational efficiency. Among the three cases listed in this work, the speedup value of the 2.5D-PD model is approximately between 103.0× and 143.3×. As the truncation thickness t_0 increases, this speedup value increases.

6.2 Verification of the bond fatigue failure condition

On the basis of the bond fatigue failure condition of the turnout rail material shown in Eq. (8), the sample loading PD model established in Section 3.2 was used to simulate the crack

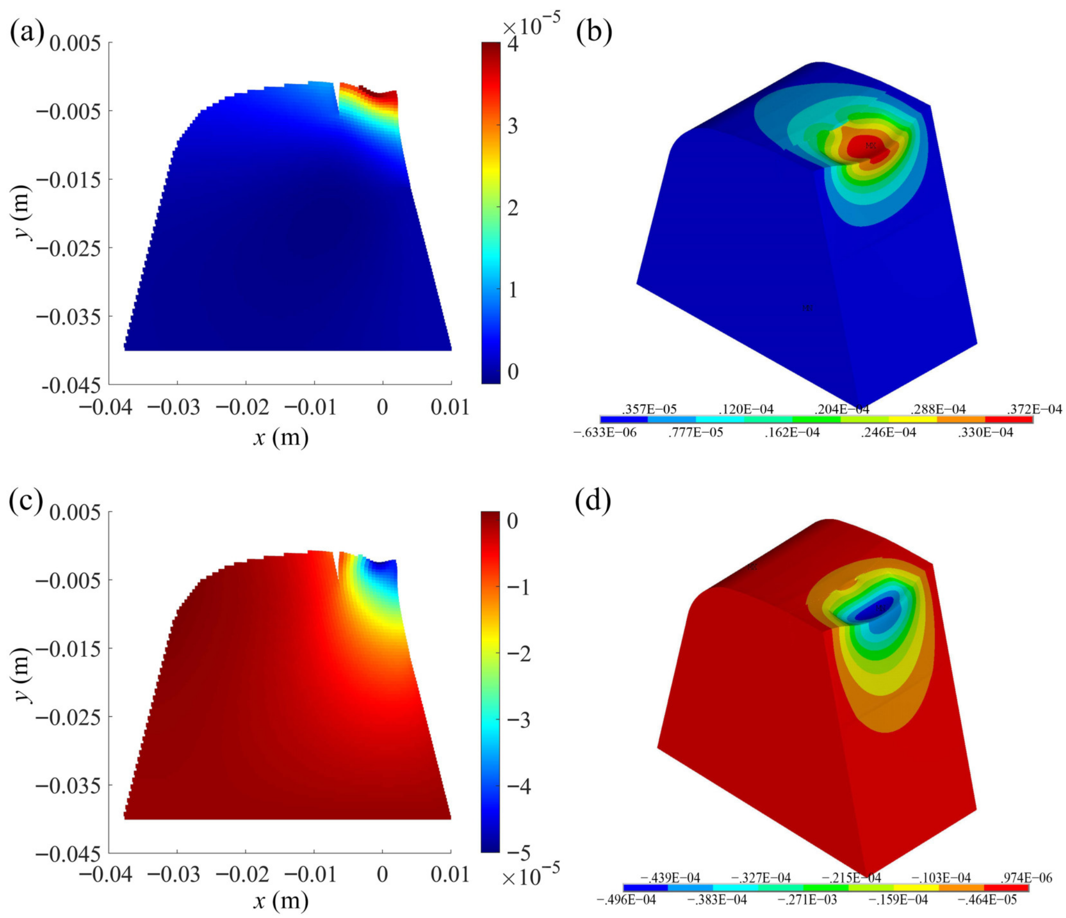

Fig. 21 Displacement results for b_0 = 5 mm and t_0 = 25 mm (unit: m): (a) lateral displacement of 2.5D-PD model, (b) lateral displacement of 3D-FEM model, (c) vertical displacement of 2.5D-PD model, and (d) vertical displacement of 3D-FEM model.

Table 3 Comparison of maximum displacements

Case	Maximum lateral displacement (m)			Maximum vertical displacement (m)		
	3D-FEM	PD-2.5D	Error (%)	3D-FEM	PD-2.5D	Error (%)
b_0 = 3 mm, t_0 = 30 mm	3.86×10^{-5}	3.80×10^{-5}	−1.55	-5.22×10^{-5}	-5.23×10^{-5}	0.19
b_0 = 5 mm, t_0 = 30 mm	4.03×10^{-5}	4.32×10^{-5}	7.20	-5.23×10^{-5}	-5.27×10^{-5}	0.76
b_0 = 5 mm, t_0 = 25 mm	3.72×10^{-5}	4.01×10^{-5}	7.80	-4.96×10^{-5}	-5.01×10^{-5}	1.00

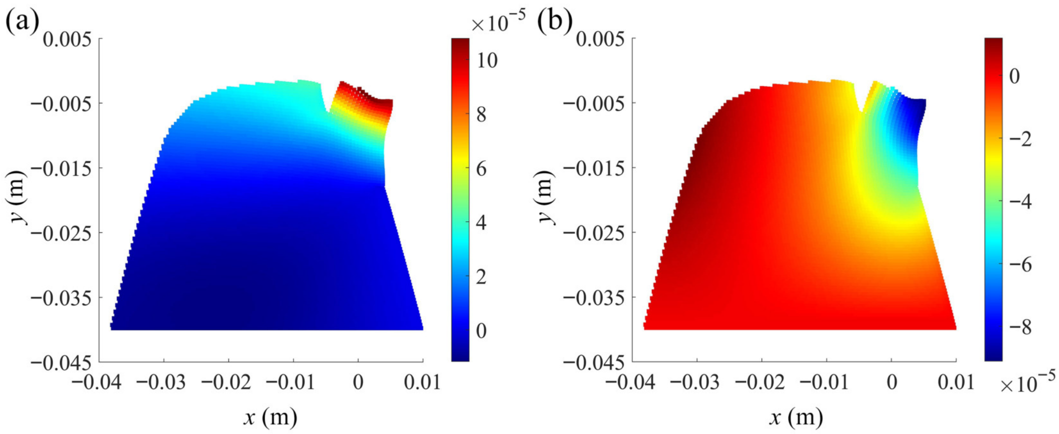

Fig. 22 Displacement results for 2D-PD model without constraints (unit: m): (a) lateral displacement, (b) vertical displacement.

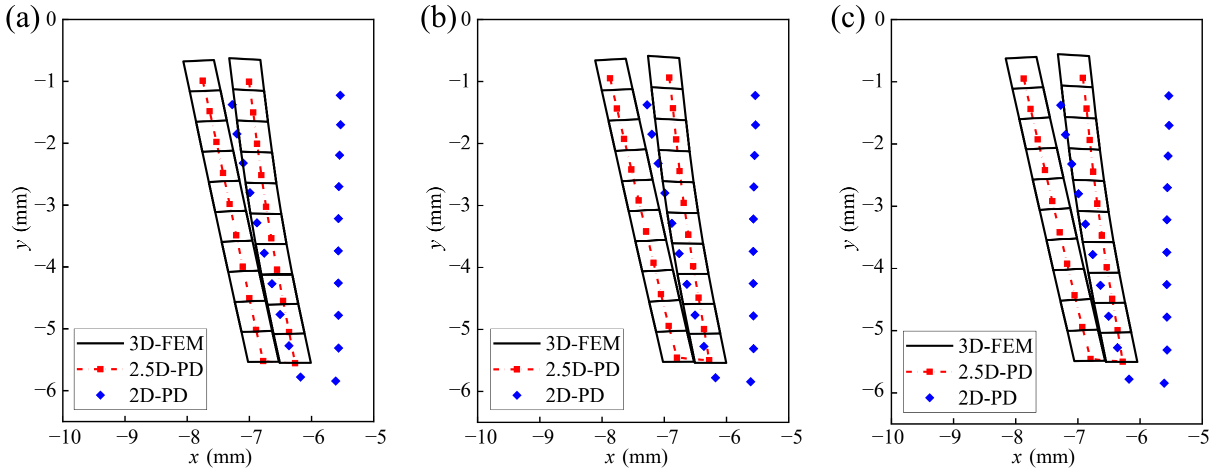

Fig. 23 Comparison of crack opening states using different models: (a) b_0 = 3 mm, t_0 = 30 mm; (b) b_0 = 5 mm, t_0 = 30 mm; (c) b_0 = 5 mm, t_0 = 25 mm.

Table 4 Comparison of computation time

Case	Node (particle number)		Computation time (min)		Speedup
	3D-FEM	PD-2.5D	3D-FEM	PD-2.5D	PD-2.5D
b_0 = 3 mm, t_0 = 30 mm	396,889	5,824	458.6	3.2	143.3×
b_0 = 5 mm, t_0 = 30 mm	396,889	5,824	466.2	3.4	137.1×
b_0 = 5 mm, t_0 = 25 mm	331,809	5,824	319.3	3.1	103.0×

propagation of the sample at a maximum load P_{max} of 15 kN and load ratio R of 0.1; the results are shown in Fig. 24.

The crack propagation length q of a sample changes with the number of loading cycles N (Fig. 25). As shown in Fig. 25, the PD simulation results are in good agreement with the experimental results, verifying the accuracy of the bond fatigue failure condition of the turnout rail material for the turnout proposed in this work.

6.3 Simulation accuracy

The crack propagation process based on the 2.5D-PD model established in this work for simulating crack propagation in the switch rail of a turnout is shown in Fig. 26. In the model, the initial crack length q_0 is 2 mm, and the crack is located 15 mm from the apex of the working edge of the switch rail, with an initial angle β of 30° and a longitudinal crack width b_0 of 3 mm. The loading conditions for the model are the same as those used in Section 6.1, whereas the wheel–rail contact state changes to a creep state (creep rate, 3×10^{-3}).

As shown in Fig. 26, as the number of loading cycles increases, cracks gradually spread to the inside of the switch rail. During this process of crack propagation, secondary cracks appear on the left side of the initial crack. Branch cracks also appear during the propagation of the main crack, a phenomenon similar to that observed in the cracks (blue line) that appeared on the onsite switch rail, as shown in Fig. 27(b). In addition, the propagation angles of the main crack increase gradually as they spread to the inside of the switch rail. As shown in Fig. 27(b), the boundary (red line) between the fatigue area and the final crack rupture area in the onsite switch rail also shows that the expansion angle gradually increases. A comparison of the simulation and observation results for the switch rail section reveals that the 2.5D-PD model established in this work can effectively simulate the rail crack propagation process in railway turnouts.

The relationships between the lengths of the extracted cracks (main crack, secondary crack, and branch crack) and the number of wheel load cycles are shown in Fig. 28. The propagation rate for the main crack is divided into three stages: They expand fastest in stage I; in stage II, their propagation rate decreases because of the

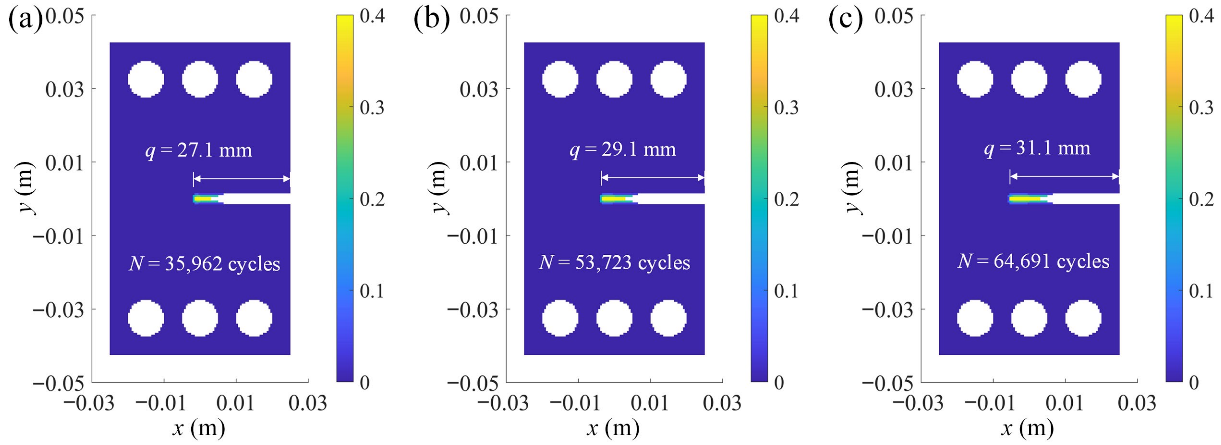

Fig. 24 PD simulation results for crack propagation of samples (P_{max} = 15 kN, R = 0.1).

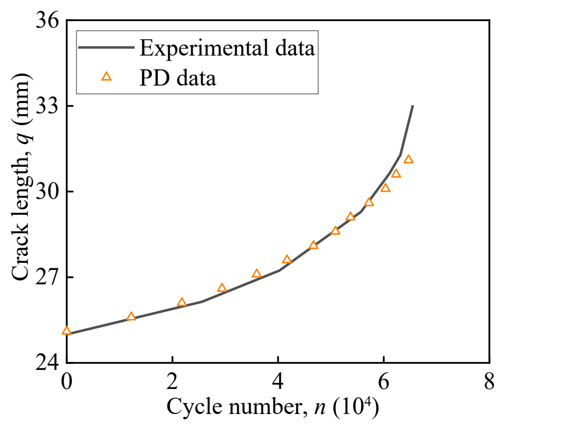

Fig. 25 Comparison of simulation and experimental results for crack propagation (P_{max} = 15 kN, R = 0.1).

emergence of a secondary crack; and in stage III, their expansion rate decreases further because of the emergence of branch cracks. The reason for this phenomenon is that as new cracks (secondary cracks and branch cracks) expand, the energy that causes the propagation of the main cracks decreases, resulting in a decrease in the propagation rate.

6.4 Impact of model length

To analyze the impact of the model length l on the calculation accuracy, a comparative analysis was performed on three cases of crack propagation simulation: (i) l = 10 mm ($l < 2a$); (ii) l = 13.84 mm ($l = 2a$); (iii) l = 20 mm ($l > 2a$), where $2a$ is the total length of the wheel–rail contact spot. The simulation results of the crack propagation paths in three different cases are shown in Fig. 29.

As shown in Fig. 29, when the model length $l < 2a$, owing to the inability to fully reflect the moving contact action of the wheel

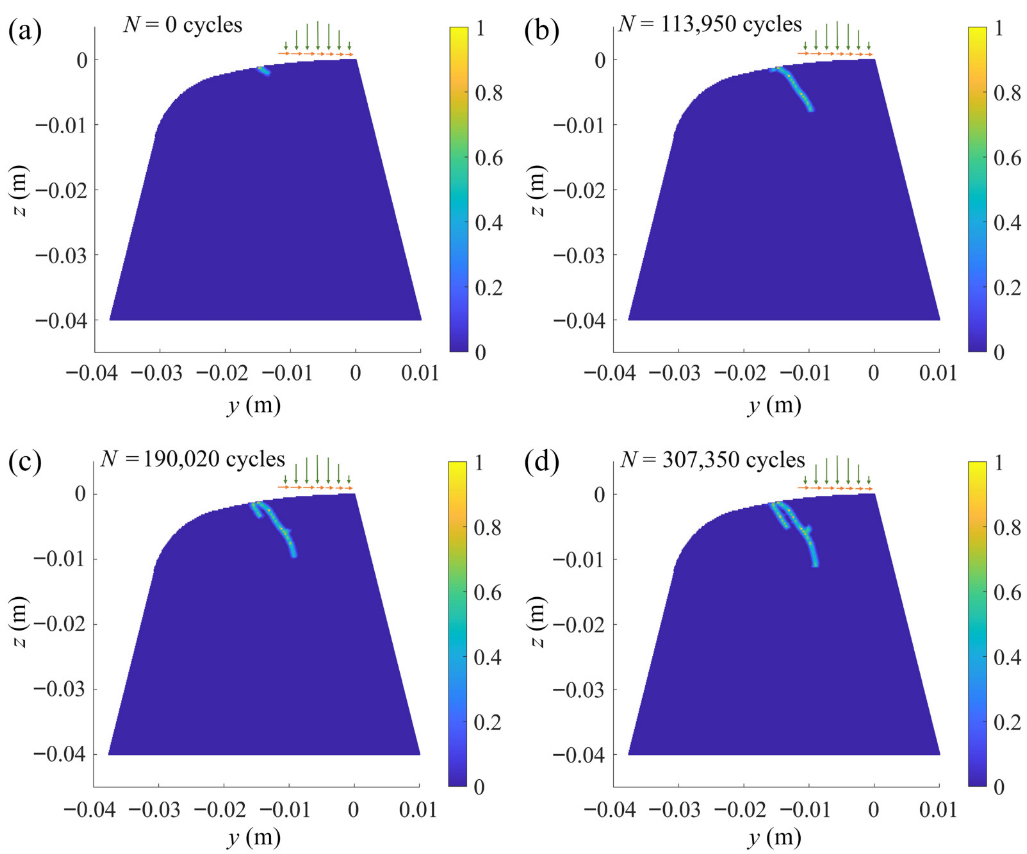

Fig. 26 2.5D-PD simulation results for switch rail crack propagation in railway turnout.

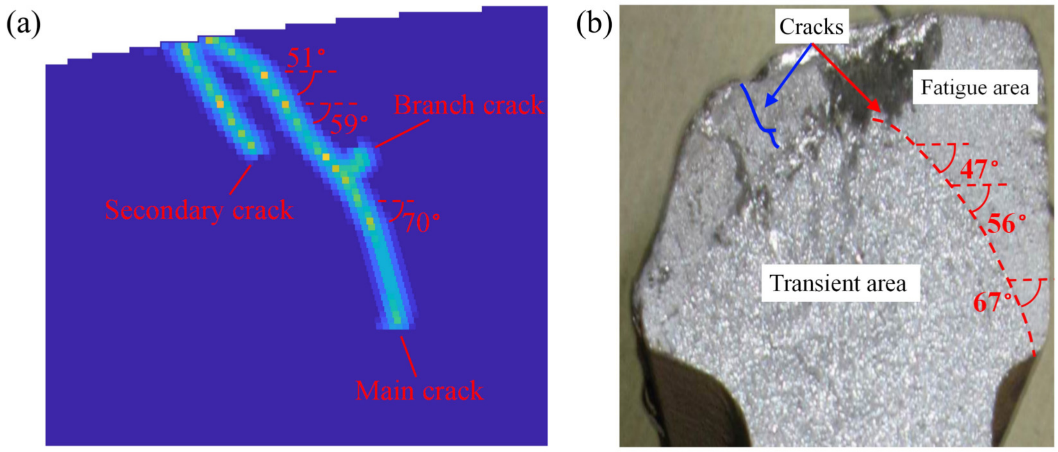

Fig. 27 Comparison of the simulated and observed crack propagation characteristics of switch rail: (a) simulated results; (b) observed results.

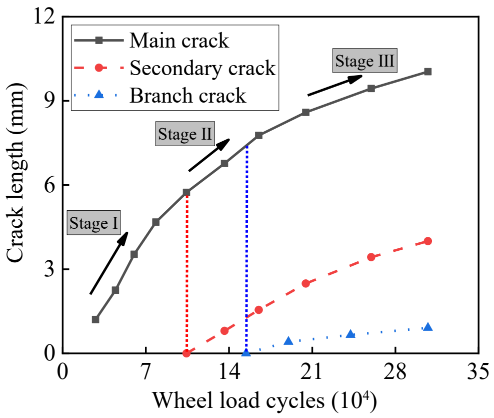

Fig. 28 Crack propagation length vs. number of wheel load cycles.

on the model, the simulation result of the crack propagation path differs significantly from the results of the other two cases. The variation in the main crack length with the number of wheel load cycles for different model lengths is shown in Fig. 30.

As shown in Fig. 30, a larger model length reduces the calculation accuracy of the crack propagation length. The reason for this phenomenon is that the deformation of the model is mainly concentrated in the area of wheel contact action (Figs. 19–21), and a larger model length will falsely increase the deformation resistance of the structure. Based on the above analysis, in the process of establishing the 2.5D-PD model, the length of the model is suggested to be consistent with the total length of the wheel–rail contact spot ($l = 2a$).

7 Conclusions

Numerous fatigue failures related to crack propagation can occur in the switch rail of a railway turnout. Rail fatigue failure of turnouts significantly increases maintenance costs and poses a direct threat to the safety of vehicle operation. Classical continuum mechanics theory has limitations in solving the problem of crack propagation. Therefore, a 2.5-dimensional (2.5D)-peridynamics (PD) model for simulating rail crack propagation in a turnout was proposed in this work based on PD theory; this model is more suitable for solving discontinuous problems such as crack propagation.

A 2D-PD model was constructed to simulate rail crack propagation in railway turnouts, and two types of 2.5D additional constraints on the crack opening and cross section were proposed to reflect the constraint effects of the 3D structure on the 2D model. A fatigue crack propagation rate experiment with U71Mn rail material in a railway turnout was conducted. The bond fatigue failure conditions of the turnout rail material were constructed and verified by comparison with the experimental results. The accuracy of the 2.5D-PD model for simulating structural deformation was verified by comparison with that of the 3D-FEM model. The simulation results for rail crack propagation were compared with the results observed on site, with crack bifurcation characteristics and propagation angle rules found to be similar across the simulated and field observation results. These findings indicate that the proposed 2.5D-PD model can effectively simulate the rail crack propagation process in railway turnouts.

The main innovations of this work are reflected in the following two aspects. On the one hand, two types of 2.5D additional constraints were proposed and verified. These additional constraints can reflect the constraint effects of the 3D structure on the 2D model. On the other hand, a 2.5D peridynamic model for rail crack propagation in railway turnouts was established. This model can be used to predict the propagation path and life of turnout rail cracks, which is highly important for the maintenance of railway turnouts.

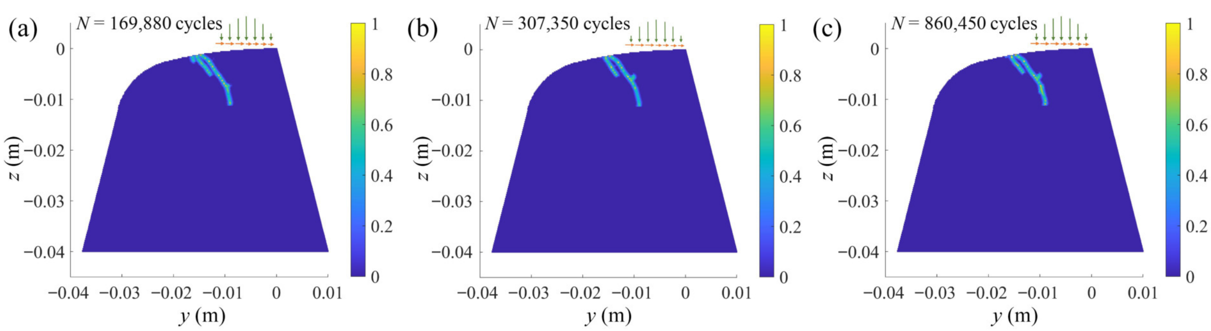

Fig. 29 Simulation results of crack propagation paths with different model lengths: (a) $l = 10$ mm ($l < 2a$); (b) $l = 13.84$ mm ($l = 2a$); (c) $l = 20$ mm ($l > 2a$).

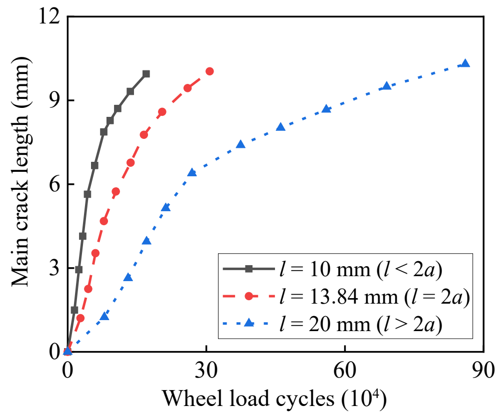

Fig. 30 Main crack length with number of wheel load cycles for different model lengths.

The crack propagation model for turnout rails proposed in this work still has several limitations. For example, the crack in this model is assumed to be a planar crack with the same longitudinal width b_0. However, the longitudinal width of a crack usually gradually decreases from the surface to the interior of the rail [43]. Therefore, there are several limitations in applying this model to solve such crack propagation problems. In addition, some rails in railway turnouts are not attached to other rails. Therefore, the boundary conditions of the prediction model must be modified accordingly to ensure the validity of the calculation results.

In this work, some interesting phenomena, such as secondary cracks and branch cracks, occurred during the simulation process. To explain the causes of these phenomena, the necessary conditions for the formation of secondary cracks and branch cracks will be studied further in future work. In addition, the interaction of multiple cracks during propagation after secondary cracks and branch cracks occurring will also be studied.

Acknowledgements

The authors acknowledge the support of the National Natural Science Foundation of China (Nos. 52108406, 52368060, and 52272348), Jiangxi Natural Science Foundation (No. 20232ACB214010), Jiangxi Double Thousand Project (No. jxsq2023201084), Project of State Key Laboratory of Performance Monitoring and Protecting of Rail Transit Infrastructure (No. HJGZ2023202), and the Key Research and Development Plan of Jiangxi Province (No. 20223BBE51009).

Availability of data and materials

The data that support the findings of this study are available from the corresponding author upon reasonable request.

Declaration of competing interest

The authors have no competing interests to declare that are relevant to the content of this article.

References

[1] Zuo Y, Lundberg J, Najeh T, Rantatalo M, Odelius J. Squat detection of railway switches and crossings using point machine vibration measurements. *Sensors* **23**(7): 3666 (2023)

[2] Zuo Y, Thiery F, Chandran P, Odelius J, Rantatalo M. Squat detection of railway switches and crossings using wavelets and isolation forest. *Sensors* **22**(17): 6357 (2022)

[3] Cornish A, Smith R A, Dear J. Monitoring of strain of in-service railway switch rails through field experimentation. *P I Mech Eng F—J RaI* **230**(5): 1429–1439 (2016)

[4] Wang S G, Wang H Y, Jing G Q. Experimental analysis of profile degradation of high-speed turnouts: A case study in China. *Tribol Int* **178**: 108035 (2023)

[5] Luo Q S, Kitchen M, Li J B, Li W B, Li Y Z. Experimental investigation on the spalling failure of a railway turnout made from Hadfield steel. *Wear* **523**: 204779 (2023)

[6] Zhang F C, Lv B, Zheng C L, Zou Q, Zhang M, Li M, Wang T S. Microstructure of the worn surfaces of a bainitic steel railway crossing. *Wear* **268**(11–12): 1243–1249 (2010)

[7] Eck S, Oßberger H, Oßberger U, Marsoner S, Ebner R. Comparison of the fatigue and impact fracture behaviour of five different steel grades used in the frog of a turnout. *P I Mech Eng F—J RaI* **228**(6): 603–610 (2014)

[8] Guo S L, Sun D Y, Zhang F C, Feng X Y, Qian L H. Damage of a Hadfield steel crossing due to wheel rolling impact passages. *Wear* **305**(1–2): 267–273 (2013)

[9] Zhu X X, Xu J M, Li Y, Hou M Y, Qian Y, Wang P, Chen J Y, Yan Z. Load spectrum extrapolation method for fatigue damage of the turnout based on kernel density estimation. *Eng Fail Anal* **160**: 108169 (2024)

[10] Ma X C, Wang P, Xu J M, Chen R, Liu L Y. Numerical simulation of rail surface-initiated rolling contact fatigue in the switch panel of railway turnouts. *P I Mech Eng F—J RaI* **235**(2): 155–165 (2021)

[11] Six K, Sazgetdinov K, Kumar N, Müller G, Velic D, Daves W, Skrypnyk R, Pålsson B A. A whole system model framework to predict damage in turnouts. *Veh Syst Dyn* **61**(3): 871–891 (2023)

[12] Qian Y, Wang P, Chen J Y, Bethel Lulu G, Xu J M, An B Y. Numerical investigation of the influence of the creep curve on the wheel–rail contact damage in high-speed railway turnouts. *P I Mech Eng F—J RaI* **233**(9): 926–936 (2019)

[13] Nielsen J C O, Pålsson B A, Torstensson P T. Switch panel design based on simulation of accumulated rail damage in a railway turnout. *Wear* **366–367**: 241–248 (2016)

[14] Xin L, Markine V L, Shevtsov I Y. Numerical procedure for fatigue life prediction for railway turnout crossings using explicit finite element approach. *Wear* **366–367**: 167–179 (2016)

[15] Silling S A. Reformulation of elasticity theory for discontinuities and long-range forces. *J Mech Phys Solids* **48**(1): 175–209 (2000)

[16] Ma X C, Yin W B, Wang Y J, Liu L Y, Wang X H, Qian Y. Fatigue failure analysis of U75V rail material under Ⅰ+Ⅱ mixed-mode loading: Characterization using peridynamics and experimental verification. *Int J Fatigue* **185**: 108371 (2024)

[17] Freimanis A, Kaewunruen S. Peridynamic analysis of rail squats. *Appl Sci* **8**(11): 2299 (2018)

[18] Ding H H, Li J C, Cui X L, Xiao Q, Guo J, Liu Q Y, Wang W J, Zhou Z R. Peridynamic simulationons of RCF crack growth in laser quenched rail material. *Eng Fract Mech* **269**: 108520 (2022)

[19] Ma X C, Wang Y J, Wang X H, Yin W B, Liu L Y, Xu J M. Investigation on fatigue crack propagation behaviour of U71Mn and U75V rails using peridynamics. *Eng Fract Mech* **281**: 109097 (2023)

[20] Ma X C, Xu J H, Liu L Y, Wang P, Feng Q S, Xu J M. A 2D peridynamic model for fatigue crack initiation of railheads. *Int J Fatigue* **135**: 105536 (2020)

[21] Ma X C, Wang L, Xu J H, Feng Q S, Liu L Y, Chen H P. A two-dimensional ordinary state-based peridynamic model for surface fatigue crack propagation in railheads. *Eng Fract Mech* **265**: 108362 (2022)

[22] Wang X M, Wang Q H, An B Y, He Q, Wang P, Wu J. A GPU parallel scheme for accelerating 2D and 3D peridynamics models. *Theor Appl Fract Mech* **121**: 103458 (2022)

[23] Wang X M, Ma S N, Dong W J, Zhao X, An B Y, He Q, Ding H H, Wang P, Wang W J. Peridynamic modeling of rail wear during sliding contact considering thermal effects. *Wear* **532–533**: 205110 (2023)

[24] Ma X C, Wang Y J, Liu L Y, Yin W B, Wang X H, Lin H S, Yu L, Shi Q F, Xu J M. A peridynamic model for rail crack initiation with cavity defect. *Tribol Int* **191**: 109116 (2024)

[25] Hamarat M, Papaelias M, Kaewunruen S. Fatigue damage assessment of complex railway turnout crossings via Peridynamics-based digital twin. *Sci Rep* **12**(1): 14377 (2022)

[26] Silling S A, Epton M, Weckner O, Xu J, Askari E. Peridynamic states and constitutive modeling. *J Elast* **88**(2): 151–184 (2007)
[27] Zhang H, Qiao P Z. A two-dimensional ordinary state-based peridynamic model for elastic and fracture analysis. *Eng Fract Mech* **232**: 107040 (2020)
[28] Silling S A, Askari E. A meshfree method based on the peridynamic model of solid mechanics. *Comput Struct* **83**(17–18): 1526–1535 (2005)
[29] Silling S A, Askari A. Peridynamic model for fatigue cracking. Tech. rep. no. SAND-18590. Albuquerque, NM: Sandia National Laboratories (SNL-NM), 2014.
[30] Zhong W, Hu J J, Li Z B, Liu Q Y, Zhou Z R. A study of rolling contact fatigue crack growth in U75V and U71Mn rails. *Wear* **271**(1–2): 388–392 (2011)
[31] Wang Y Q, Zhou H, Shi Y J, Feng B R. Mechanical properties and fracture toughness of rail steels and thermite welds at low temperature. *Int J Miner Metall Mater* **19**(5): 409–420 (2012)
[32] Nguyen C T, Oterkus S, Oterkus E. An energy-based peridynamic model for fatigue cracking. *Eng Fract Mech* **241**: 107373 (2021)
[33] Fang X Y, Zhang H N, Ma D W. Influence of initial crack on fatigue crack propagation with mixed mode in U71Mn rail subsurface. *Eng Fail Anal* **136**: 106220 (2022)
[34] Sun H D, Wang Z H, Wang P, Chen C H, Jin X, Zhao X J, Ren R M, Li Z M, Zhang H W. An investigation on the formation and hardening mechanisms of white etching layer in hypoeutectoid rail surface. *Wear* **530**: 205010 (2023)
[35] Lesiuk G, Smolnicki M, Mech R, Zięty A, Fragassa C. Analysis of fatigue crack growth under mixed mode (I + II) loading conditions in rail steel using CTS specimen. *Eng Fail Anal* **109**: 104354 (2020)
[36] Richard H A. Bruchvorhersagen bei überlagerter normal-und schubbeanspruchung von rissen. Düsseldorf: VDI-Verlag, 1985. (in German)
[37] Ren H L, Zhuang X Y, Cai Y C, Rabczuk T. Dual-horizon peridynamics. *Int J Numer Meth Engng* **108**(12): 1451–1476 (2016)
[38] Shojaei A, Mossaiby F, Zaccariotto M, Galvanetto U. An adaptive multi-grid peridynamic method for dynamic fracture analysis. *Int J Mech Sci* **144**: 600–617 (2018)
[39] Silling S A. EMU user's manual, Code Ver. 2.6d. Albuquerque, NM: Sandia National Laboratories (SNL-NM), 2004.
[40] Hertz H. Ueber die berührung fester elastischer körper. *J Reine Angew Math* **92**(1882): 156–171 (1882) (in German)
[41] Johnson K L. The effect of a tangential contact force upon the rolling motion of an elastic sphere on a plane. *J Appl Mech* **25**(3): 339–346 (1958)
[42] Kilic B, Madenci E. An adaptive dynamic relaxation method for quasi-static simulations using the peridynamic theory. *Theor Appl Fract Mech* **53**(3): 194–204 (2010)
[43] Wang S F, Zhang L S, Qian Y, Zhou Y. Portray rail head surface crack 3D contour through image analysis and morphology reconstruction. *Eng Fail Anal* **151**: 107374 (2023)

Xiaochuan Ma received his Ph.D. degree from Southwest Jiaotong University, Chengdu, China, in 2018. He is now a full professor at the East China Jiaotong University, Nanchang, China. His research interests include fatigue damage behavior of turnout rails, wheel rail rolling contact mechanics, and vehicle-turnout system dynamics.

Xianghe Wang received his bachelor degree from East China Jiaotong University, Nanchang, China, in 2021. He is a postgraduate student at East China Jiaotong University, Nanchang, China. His research interests include fatigue damage behavior of turnout rails and vehicle-turnout system dynamics.

Linya Liu received his Ph.D. degree from Tongji University, Shanghai, China, in 2006. He is now a full professor at the East China Jiaotong University, Nanchang, China. His research interests include safety and maintenance of rail transit infrastructure, vibration, and noise of rail transit.

Weibin Yin received his bachelor degree from East China Jiaotong University, Nanchang, China, in 2018. He is a postgraduate student at East China Jiaotong University. His research interest is fatigue fracture characteristics of rail materials.

Yajie Wang received her bachelor degree from Suzhou University of Science and Technology, Suzhou, China, in 2022. She is now a postgraduate student at East China Jiaotong University, Nanchang, China. Her research interest is fatigue damage behavior of rails considiering void defect.

Qi Zeng received her bachelor degree from Xinxiang University, Xinxiang, China, in 2023. She is now a postgraduate student at East China Jiaotong University, Nanchang, China. Her research interest is rolling contact fatigue damage behavior of rails.